




# Investigation of the structural and magnetic properties of rapidly solidified Nd–Fe–B–Ce alloys

Orkun Aytekin<sup>1</sup>, Rifat Kurban<sup>2</sup>, Ali Durmuş<sup>3</sup>, Hakan Çolak<sup>4</sup>, and Ercan Karaköse<sup>5,\*</sup> 

<sup>1</sup> Department of Graduate Education Institute, Electrical-Electronics Engineering, Kayseri University, Kayseri, Turkey

<sup>2</sup> Department of Computer Engineering, Engineering Faculty, Abdullah Gul University, Kayseri, Turkey

<sup>3</sup> Department of Electrical and Electronics Engineering, Engineering & Architecture and Design Faculty, Kayseri University, Kayseri, Turkey

<sup>4</sup> Department of Chemistry, Faculty of Science, Çankırı Karatekin University, 18100 Çankırı, Turkey

<sup>5</sup> Department of Natural Sciences, Engineering & Architecture and Design Faculty, Kayseri University, Kayseri, Turkey

**Received:** 29 November 2023

**Accepted:** 14 July 2024

**Published online:**

30 July 2024

© The Author(s), 2024

## ABSTRACT

This study introduces the first literature report of rapidly solidified Nd–Fe–B–Ce alloys fabricated using the melt-spinning technique at varying disc rotation speeds. The resulting alloy images are then analyzed using various image processing techniques, and their structural and magnetic characteristics are described. The alloys are characterized using a variety of methods, including x-ray diffraction (XRD), field-emission scanning electron microscopy (FE-SEM), energy-dispersive x-ray spectroscopy (EDX), differential thermal analysis (DTA), vibrating sample magnetometry (VSM), and Vickers microhardness tests. By using XRD, the tetragonal hard magnetic Nd<sub>2</sub>Fe<sub>14</sub>B phase is detected in the Nd<sub>30</sub>Fe<sub>65</sub>B<sub>0.9</sub>Ce<sub>5</sub> alloy. The FE-SEM microstructure analysis shows that the grain structure of the ingot alloy is indistinct, and the tetragonal symmetric structure begins to appear at disc rotation speeds of 20 m/s and 40 m/s. The analysis of FE-SEM images using histogram analysis, the image segmentation technique, and VSM method reveals that the coercivity values of the sample produced at the 80 m/s solidification speed increased by approximately 34% when compared to the ingot alloy.

## 1 Introduction

As energy resources decrease, energy efficiency practices are becoming more widespread. With the increase in energy usage worldwide, the efficient use of energy has emerged as a separate area of expertise. The quality of permanent magnets is very important when considering efficiency in generator and motor technologies. Due to their great energy efficiency and low price,

Nd–Fe–B magnets are widely used in many applications, including hard disc drives, voice coil motors, hybrid, and electric automobiles. It has become very important to reduce the eddy current loss, which is observed in electric motors and reduces the efficiency considerably. Because the electrical resistance of Nd–Fe–B magnets is relatively low, magnetic field loss due to eddy current loss is often observed under working conditions and wear. This loss can be limited

Address correspondence to E-mail: ercankarakose@gmail.com

by adding different elements to Nd–Fe–B magnets and using production methods that prevent oxidation. Another advantage of these magnets is that they have a high anisotropy field and a large saturation magnetization. As a result of intensive research in the last decades, Nd–Fe–B magnets have become available for practical use with maximum energy production and high efficiency. The magnetic properties and electrical resistance of Nd–Fe–B magnets depend on their microstructures, especially the grain size of the Nd–Fe–B alloy. Rare earth metal-based Nd–Fe–B type magnetic alloys are widely utilized as permanent magnets in various applications due to their integrated structure, lightness, small size, and high maximum energy product BH (max).

In recent years, permanent magnet applications have rapidly expanded in the industrial, transportation, information, and automation technology industries [1–3]. Nd–Fe–B magnets have higher magnetic properties than other rare earth element-based magnets. They are also lighter, have a higher mechanical strength, and are less expensive [4]. Special conditions are required to operate hard magnets at higher temperatures. Decreasing coercivity ( $H_c$ ) makes the magnets more sensitive during the demagnetization process. Therefore, heavy rare earth elements like terbium (Tb) and dysprosium (Dy) are necessary for high-temperature applications [5, 6]. Cerium (Ce), one of the most abundant rare earth elements in nature, offers a promising alternative for Nd/Pr/Dy in 2:14:1-type permanent magnets. The potential of Ce to reduce magnet production costs and decrease the demand for other rare earth elements has increased interest in this element. The lower intrinsic magnetic properties of sintered  $Ce_2Fe_{14}B$  ( $J_s$ : 1.17 T,  $H_A$ : 2.6 T,  $T_C$ : 151 °C) compared to  $Nd_2Fe_{14}B$  ( $J_s$ : 1.6 T,  $H_A$ : 7.3 T,  $T_C$ : 351 °C), due to the excessive substitution of Nd by Ce, significantly diminish the overall magnetic characteristics [7–9]. With the increasing Ce ratio, the  $CeFe_2$  phase, which has a negative effect on the magnetic properties, emerges, and the Ce ratio should be below 6.85 wt% to minimize the negative effect on the magnetic properties. In recent studies, it has been shown that adding Ce to Nd-based magnets can increase the coercivity [10, 11]. Therefore, optimizing the sintered Nd–Fe–B–Ce magnets is crucial [12, 13]. Many researchers have extensively studied the behavior of permanent magnets at various temperatures in recent years. Attempts have been made to enhance the magnetic properties of Nd–Fe–B by improving its thermal

stability [14–16]. Additionally, the effects of adding Ce and La to Nd–Fe–B permanent magnets to basic magnetic parameters at high temperatures have been studied and the magnetic properties were investigated in the range of 480 to 1080 °C [17–19].

This study is the first to report on the use of image processing techniques for analyzing the microstructure of Nd–Fe–B–Ce alloy samples. Through this analysis, valuable information, such as the crystal structure and grain sizes of the alloy, can be obtained. The data have the potential to offer valuable insights into the effects of rapid solidification on the microstructure and magnetic behavior of the alloy. To achieve this,  $Nd_{30}Fe_{65}B_{0.9}Ce_5$  alloys were produced using the melt-spinning (MS) method at speeds of 20, 40, 60, and 80 m/s. Subsequently, the obtained alloy images were analyzed using various image processing techniques to investigate their structural and magnetic properties.

## 2 Experimental procedure

Ingot alloys with nominal compositions of Nd–65 wt.% Fe–0.9 wt.% Be–5 wt.% Ce were prepared in a vacuum induction furnace by using 99.99% pure Nd, Fe, Be, and Ce. The materials were added to an induction cast furnace and melted at a temperature of 1800 °C, then held for 150 min to ensure the diffusion and dissolution of the elements. The single-cylinder melt-spinning method was used to produce rapid solidification (RS) samples of the alloy in an argon atmosphere at room temperature. The molten alloy underwent RS by flowing it through a 1 mm diameter hole over a copper disc at velocities of 20, 40, 60, and 80 m/s. They were annealed in an argon environment at 853 K for 60 min, to reveal the strong magnetic properties of the samples. The thickness of the resulting ribbons was measured using a micrometer and the microstructures were analyzed via cold-mounting, grinding, and polishing, followed by observation using various methods such as FE-SEM, XRD, DTA, VSM, and EDX. A LABSYS Evo DTA differential thermal analysis instrument was used to conduct the thermal analysis in an argon environment with a heating rate of 10 °C  $min^{-1}$ . The DTA analysis of  $Nd_{30}Fe_{65}B_{0.9}Ce_5$  samples was carried out using alloy strips and ingot alloys produced at different disc speeds of 20, 40, 60, and 80 m/s. To this end, each ribbon sample is cut into small pieces using scissors and 10–15 mg pieces are prepared from the strips. In addition, a controlled atmosphere is created

by providing a liquid nitrogen flow of 10 lt/min to the crucible to reduce the temperature increase and minimize the oxidation effect. The temperature control unit is set to heat the samples at a rate of 10 °C/min. The sample phase structures were analyzed via X-ray diffractometry utilizing a Panalytical Empyrean XRD diffractometer with  $\text{CuK}\alpha$  radiation at 40 kV/40 mA. The XRD analysis was conducted at  $2\theta$  angles ranging from 10° to 90° with a step size of 0.02, a scan speed of 5°/min, and a time per 50 s for phase identification. The topographies of the samples were examined at high magnifications through the utilization of a ZEISS Gemini SEM 500 for the FE-SEM analysis. The microhardness of the  $\text{Nd}_{30}\text{Fe}_{65}\text{B}_{0.9}\text{Ce}_5$  alloys was measured at 25 °C using an Emcotest Durascan 70 model hardness device with a holding time of 10 s and an applied load of 0.098, 0.245, 0.49, 0.98, 1.47, and 1.96 N. The magnetic properties of the samples were determined via VSM analysis utilizing the Lake Shore 7407 model vibrational sample magnetometer.

### 3 Results and discussion

#### 3.1 X-Ray structure analysis

Samples of the alloys were obtained using the ingot and melt-spinning methods before undergoing the XRD analysis. This process was used to examine the phase structure of the alloy. The XRD analysis results for the  $\text{Nd}_{30}\text{Fe}_{65}\text{B}_{0.9}\text{Ce}_5$  ingot alloy are illustrated in Fig. 1(a). In the  $\text{Nd}_{30}\text{Fe}_{65}\text{B}_{0.9}\text{Ce}_5$  ingot alloy, the peaks associated with a tetragonal symmetric hard magnetic  $\text{Nd}_2\text{Fe}_{14}\text{B}$  phase (space group  $\text{P4}_2/\text{mnm}$ ) were detected on planes (004), (214), (105), (115), (006), (116), (511), (008), (317), (208), (218), and (319). No peaks associated with Ce were observed in this alloy. Previous research has shown that  $\text{CeFe}_2$  phases and other Ce-related phases are not detected in Nd–Ce–Fe–B when the Ce content is below the critical value of 21.5 at.% [10, 20]. Also, the Ce-based lattice constants in the  $\text{RE}_2\text{Fe}_{14}\text{B}$  phase ( $a = b = 0.876$  nm,  $c = 1.211$  nm) were lower than those of the Nd-based lattice constants ( $a = b = 0.880$  nm,  $c = 1.220$  nm) [21, 22].

Figure 1b, c, d, e shows the XRD analysis peaks of the MS  $\text{Nd}_{30}\text{Fe}_{65}\text{B}_{0.9}\text{Ce}_5$  alloys at disc speeds of 20, 40, 60, and 80, respectively. In the samples of  $\text{Nd}_{30}\text{Fe}_{65}\text{B}_{0.9}\text{Ce}_5$  produced at 20 and 40 m/s, peaks corresponding to the  $\text{Nd}_2\text{Fe}_{14}\text{B}$  phase in a tetragonal structure on (004), (214), (105), (115), (006), (116),

(511), (008), (317), (208), (218), and (319) planes had been detected. The X-ray diffraction (XRD) analysis of the RS  $\text{Nd}_{30}\text{Fe}_{65}\text{B}_{0.9}\text{Ce}_5$  alloys shows that the highest peak observed is the (006) peak plane. The peak planes of the  $\text{Nd}_{30}\text{Fe}_{65}\text{B}_{0.9}\text{Ce}_5$  alloys solidified at 20 and 40 m/s were approximately similar. The (511) peak was not observed in the  $\text{Nd}_{30}\text{Fe}_{65}\text{B}_{0.9}\text{Ce}_5$  alloy solidified at 40 m/s. It was found that (004), (214), (115), (116), (317), and (218) peaks disappeared or weakened in  $\text{Nd}_{30}\text{Fe}_{65}\text{B}_{0.9}\text{Ce}_5$  alloy when the disc speed was increased from 40 to 60 m/s. The peak planes of the  $\text{Nd}_{30}\text{Fe}_{65}\text{B}_{0.9}\text{Ce}_5$  alloys solidified at 60 and 80 m/s were also similar to each other. The (319) peak was not observed in the  $\text{Nd}_{30}\text{Fe}_{65}\text{B}_{0.9}\text{Ce}_5$  alloys solidified at 80 m/s. Based on the XRD analysis, it has been determined that some peak points of the patterns have disappeared and/or weakened depending on the solidification rates. Peaks such as (004), (214), (115), (116), (511), (317), (218), and (319) have disappeared and/or weakened with varying disc speeds. This is a significant effect of rapid solidification [14, 21].

The crystal structure of the tetragonal  $\text{Nd}_2\text{Fe}_{14}\text{B}$  phase is depicted in Fig. 2. The crystal structure of the  $\text{Nd}_2\text{Fe}_{14}\text{B}$  phase has a structure similar to the Heusler crystal structure and is tetragonal in symmetry. In this structure, there are three atomic layers consisting of four atoms of the Nd, Fe, and B group elements. These layers are arranged parallel to the (001), (010), and (100) planes. This structure is used in many technological applications such as super magnets, magnetic motors, and other electromagnetic devices due to its excellent magnetic properties. Nd (two atomic sites), Fe (six atomic sites), and B (one atomic site) atoms occupy a total of nine different atomic sites. A systematic scattering electron diffraction model has been developed to determine the crystal structure of the matrix grain in Nd–Fe–B magnets.

#### 3.2 Microstructural and image processing analysis with FE-SEM

One of the key factors that affect the performance of Nd-based magnets is grain size and shape. Reducing the grain size increases the coercive field of permanent magnets. Microstructure analysis helped to identify the optimal grain size and shape to provide a balance between magnetic density and magnetic stability. Using a FE-SEM, a detailed microstructural analysis of the ingot and alloy specimens that had been RS at speeds of 20, 40, 60, and 80 m/s is performed. In the

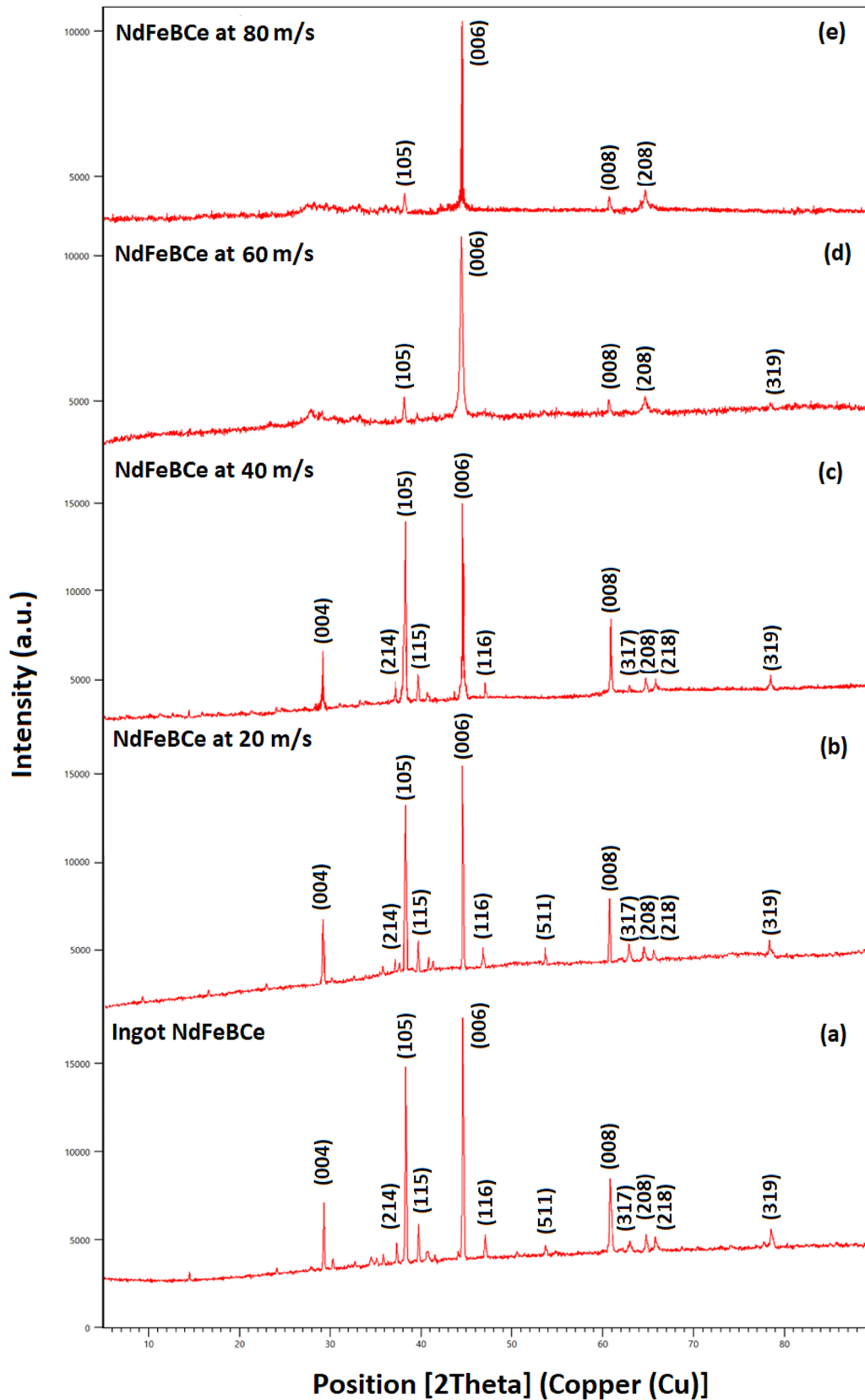


**Fig. 1** XRD peaks of  $\text{Nd}_{30}\text{Fe}_{65}\text{B}_{0.9}\text{Ce}_5$  alloy **a** ingot alloy, **b** MS 20 m/s, **c** MS 40 m/s, **d** MS 60 m/s and **e** MS 80 m/s

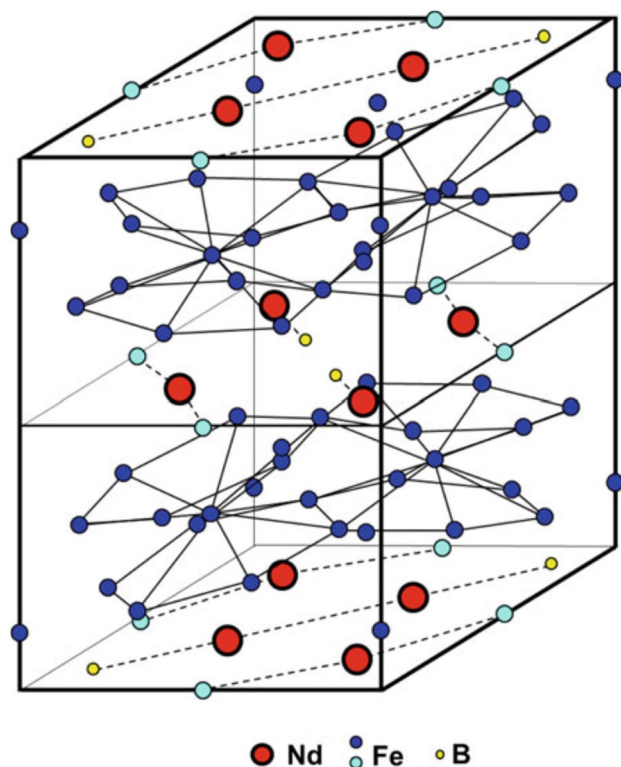


**Fig. 2** Crystal structure of the  $\text{Nd}_2\text{Fe}_{14}\text{B}$  phase with a tetragonally symmetric structure [22]

FE-SEM analyses, different magnification ratios are applied. Figure 3 a, b, c, d, e depicts, respectively, the microstructure photographs of the ingot and alloys generated at disc speeds of 20, 40, 60, and 80 m/s.

The microstructure of the ingot  $\text{Nd}_{30}\text{Fe}_{65}\text{B}_{0.9}\text{Ce}_5$  alloy has been observed to possess a non-homogeneous stacked structure. In the alloy solidified at a disc speed of 20 m/s, distinct tetragonal structures have been identified in the microstructure. Additionally, in alloys produced at disc speeds of 40, 60, and 80 m/s, tetragonal structures are also clearly visible. As the solidification speed increases, the grain boundaries become more pronounced and the microstructure becomes more homogeneous. It is noteworthy that the grain size of the RS alloy strips is smaller than that of the ingot. The tetragonal structure observed in the alloy's microstructure is likely attributed to the tetragonal strong magnet  $\text{Nd}_2\text{Fe}_{14}\text{B}$  phase. The increase in disc speed effectively improves the homogeneity of the alloy which is an effect of rapid solidification. EDX is a method that aims to determine the chemical composition of an alloy. This method determines the elements that make up a substance by measuring the energy distribution that results from the substance emitting

X-rays. The analysis of the samples was performed using EDX in conjunction with FE-SEM. In our EDX analyses, the magnification ratio was 1000, the acceleration voltage was 20 kV, and the angle of incidence of the electron beams was  $90^\circ$ . Figure 4 a, b shows the EDX analyses of the ingot and  $\text{Nd}_{30}\text{Fe}_{65}\text{B}_{0.9}\text{Ce}_5$  alloys produced at a solidification speed of 20 m/s, respectively.

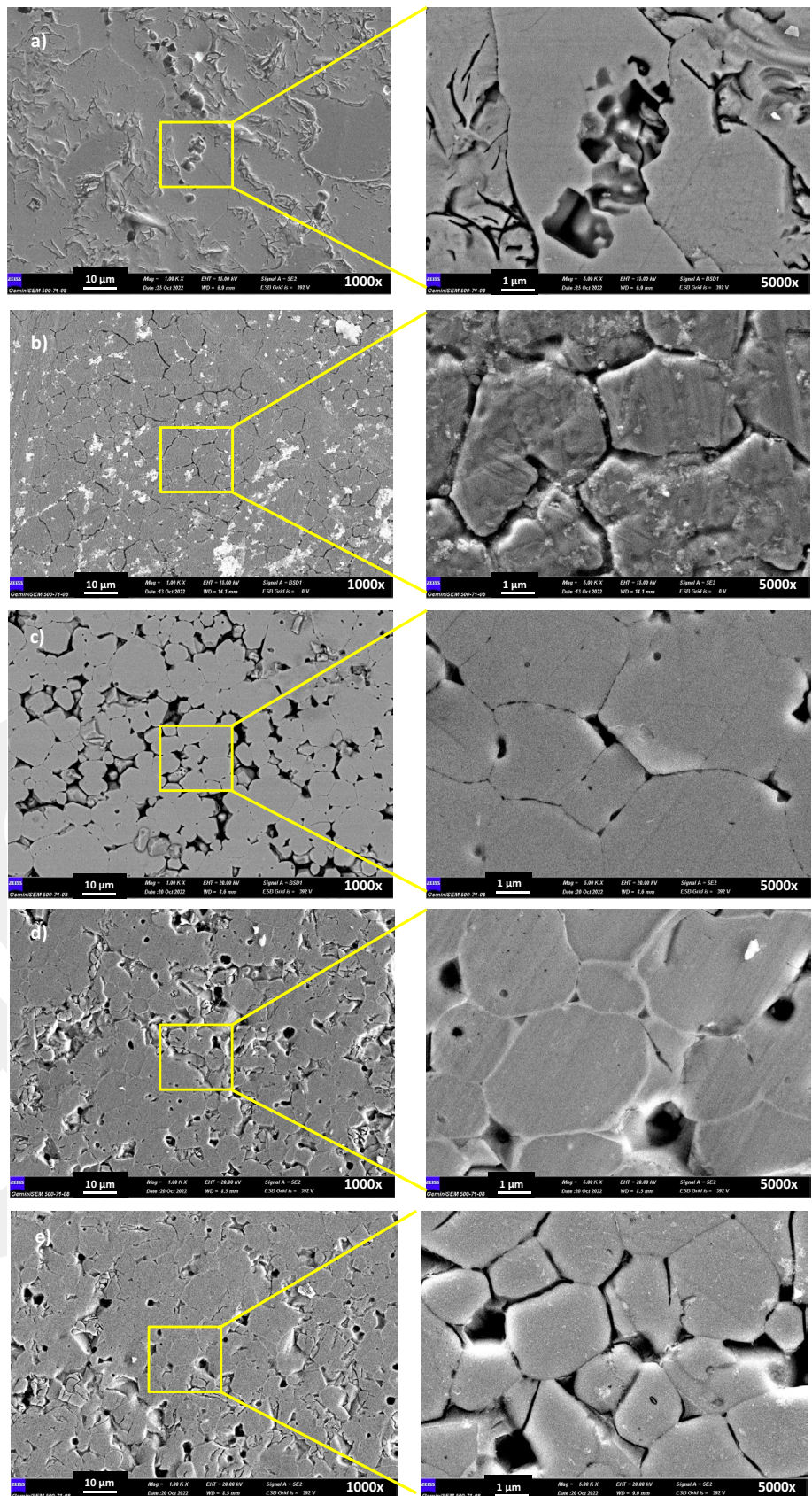
EDX analysis allows for the qualitative and quantitative determination of the elements present in an alloy. As a result of the analysis, the amounts of the elements and peak planes of Nd-Fe-Ce are obtained. The analysis revealed that the ingot alloy contained 3.32% Ce, 22.14% Nd, and 76.69% Fe. Also, the  $\text{Nd}_{30}\text{Fe}_{65}\text{B}_{0.9}\text{Ce}_5$  alloy is produced at a solidification rate of 20 m/s and it is determined that Ce is 3.48%, Nd is 21.37%, and Fe is 75.15%.

Table 1 presents the EDX analysis results of  $\text{Nd}_{30}\text{Fe}_{65}\text{B}_{0.9}\text{Ce}_5$  alloys solidified at ingot and disc speeds of 20, 40, 60, and 80 m/s. The EDX analysis indicates a decrease in the amounts of Ce and Nd elements with increasing disc speed. These results highlight the impact of solidification speed on the microstructural properties and element distribution of the alloy. In the EDX analysis, no peak for B is observed. This can be attributed to the atomic radius and the amount of the element contributed. On the other hand, EDX analysis, which determines the composition of a substance by measuring the energy distribution caused by the X-rays emitted by the substance, may not be able to detect some of the elements in the periodic system. Some of the elements' X-ray energies are lower than the detection limit of the detector, so they cannot be detected. Boron is one of the elements that cannot be detected by EDX analysis, for example. To determine the presence of Boron, different spectroscopic methods can be used.

In addition to the XRD, FE-SEM, and EDX evaluations, the results are also analyzed with the help of image processing techniques. As shown in Fig. 5, the original images (left column), the grayscale histogram of the input images (middle column), and the segmentation of these images (right column) using a marker-controlled watershed algorithm are visualized. In the image analysis, the FE-SEM images of  $\text{Nd}_{30}\text{Fe}_{65}\text{B}_{0.9}\text{Ce}_5$  ingot alloy, 20 m/s, 40 m/s, 60 m/s, and 80 m/s MS microstructure photographs magnified by 5000x were used.

An image histogram is a representation of the distribution of pixel intensities in an image. It gives

**Fig. 3** FE-SEM analysis of  $\text{Nd}_{30}\text{Fe}_{65}\text{B}_{0.9}\text{Ce}_5$  alloy **a** ingot alloy, **b** MS 20 m/s, **c** MS 40 m/s, **d** MS 60 m/s, and **e** MS 80 m/s (The microstructure photographs on the left are magnified 1000× and the microstructure photographs on the right are magnified 5000×)



**Fig. 4** FE-SEM with EDX analysis results of  $\text{Nd}_{30}\text{Fe}_{65}\text{B}_{0.9}\text{Ce}_5$  alloys **a** ingot and **b** produced at 20 m/s disc speed

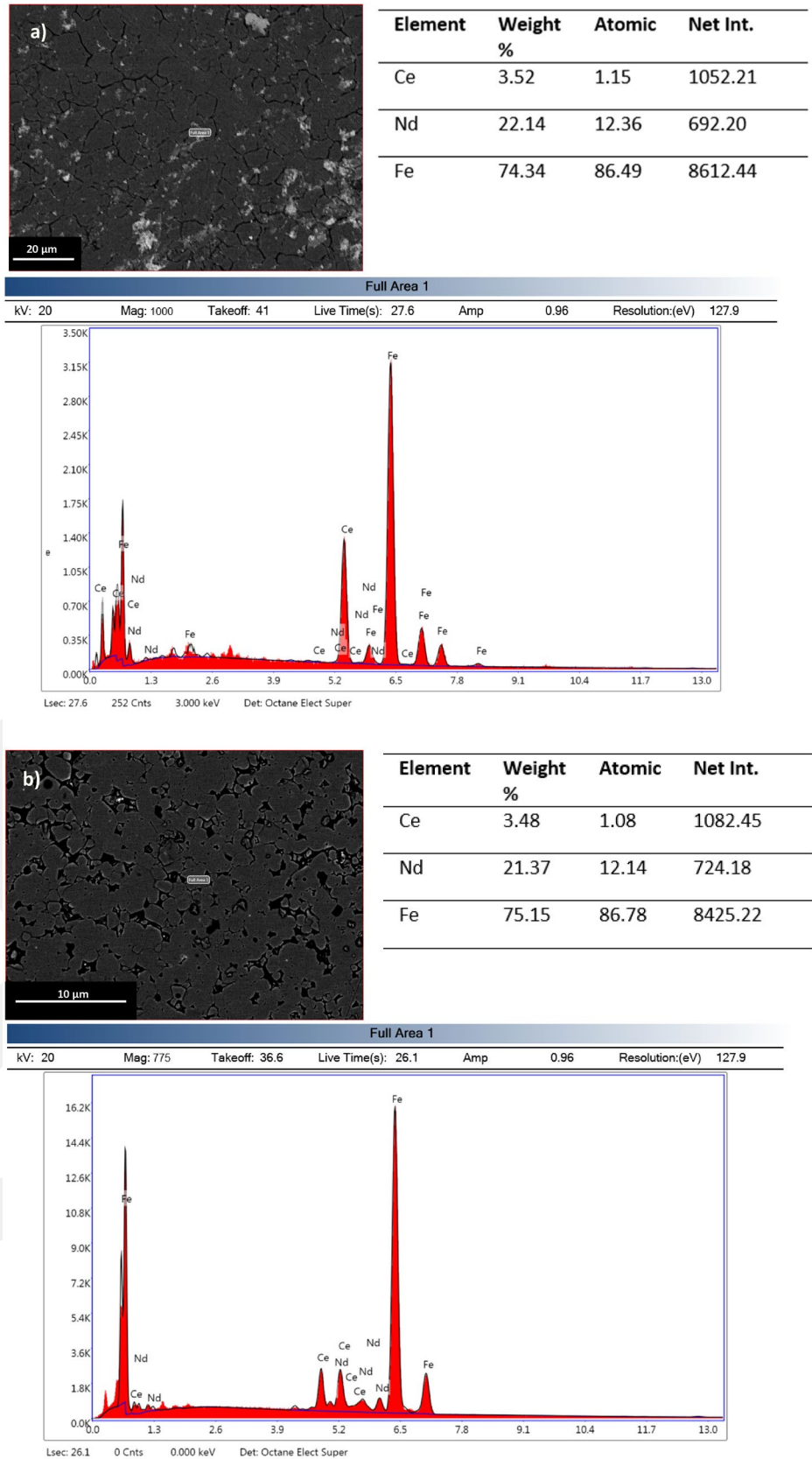


**Table 1** EDX analysis results of ingot and melt-spun  $\text{Nd}_{30}\text{Fe}_{65}\text{B}_{0.9}\text{Ce}_5$  alloys

Element	Ingot		20 m/s		40 m/s		60 m/s		80 m/s	
	Weight	Atomic	Weight	Atomic	Weight	Atomic	Weight	Atomic	Weight	Atomic
Ce	3.52	1.15	3.48	1.08	3.32	1.04	2.98	0.92	2.74	0.87
Nd	22.14	12.36	21.37	12.14	20.38	12.03	20.10	12.03	19.05	11.66
Fe	74.34	86.49	75.15	86.78	76.30	86.93	76.92	87.05	78.21	87.47

us information about the number of pixels at each intensity value in an image. The benefits of histogram analysis in image processing are that (i) it provides a simple and effective way to analyze the properties of an image, (ii) it can be used for image enhancement by adjusting the intensity values of pixels, (iii) it helps to analyze image texture and can be used for texture classification, (iv) it is a useful tool for image segmentation as it helps to identify the objects or regions of interest in an image, and (v) it can also be used for evaluating the quality of an image by comparing the histograms of two images [23, 24]. For grayscale images, a 0-pixel value means a pure black color and a 255-pixel value means a pure white color. The values between 0 and 255 represent the corresponding gray level in the gradient. As can be seen from Fig. 5, for the ingot sample, the majority of the pixels are close to the black color (0 in the x axis). For the 20 m/s sample, the pixel densities are spread over a wider range due to the texture and rough surfaces. For the 40, 60, and 80 m/s samples, the pixel densities are concentrated in a narrow color space, averaging ~ 125, ~ 140 and ~ 150 Gy level colors according to the x axis, respectively. For samples 40, 60, and 80 m/s, this analysis shows that smoother surfaces are obtained and the color brightness increased.

A watershed segmentation approach to image processing found the borders between the areas of the image that have varying intensity values by treating the image as a topographic surface. The method starts by specifying the markers that act as the initial points for the segmenting regions before building a topographic surface by converting the original image into a gradient. The segmented regions of the original image are defined by the borders between the flooded regions from the markers in the gradient image. The end result is an image that has been segmented, with each section representing a different intensity value or object from the original image [25, 26]. In Fig. 6, the steps of the marker-controlled watershed segmentation algorithm are given as an example using the 80 m/s image.

As can be seen in Fig. 5, for the ingot sample, there are no regular surface shapes. There are plenty of pits on the surface and the segmentation results are accordingly inaccurate. Although some regular hexagonal shapes were formed for the 20 m/s sample, the sample surfaces are quite rough. The segmentation results are partially correct, for example, for the large piece at the bottom right, it produced incorrect segmentations. In the 40 and 60 m/s samples, hexagonal smooth surfaces are formed. However, some of the regions are segmented together, while some regions are segmented into two parts. In the 80 m/s sample, a large number of hexagonal structures were formed and segmented with high accuracy in the visual evaluation. The histogram and segmentation analysis indicate that the  $\text{Nd}_2\text{Fe}_{14}\text{B}$  hard magnetic phase is more evident when there is an increase in disc velocity.

### 3.3 DTA analysis

The melting characteristic of the  $\text{Nd}_{30}\text{Fe}_{65}\text{B}_{0.9}\text{Ce}_5$  sample alloy is determined by the DTA analysis shown in Fig. 7. In these analyses, only one endothermic melting curve is observed. These melting peaks are measured in the range of 1123–1180 K and are attributed to the tetragonal  $\text{Nd}_2\text{Fe}_{14}\text{B}$  phase. These values are consistent with the literature and similar results have been obtained in previous studies [27–29]. Additionally, the melting peaks observed in Fig. 7 are also consistent with the peaks observed in the XRD analysis (see Figs. 1). This melting peak detected in DTA analysis belongs to the  $\text{Nd}_2\text{Fe}_{14}\text{B}$  phase [21, 30]. This compatibility shows us that the thermodynamic properties and phase structure of the alloy are consistent.

### 3.4 VSM analysis

In a magnetic system, the magnetic hysteresis curve shows the relationship between the magnetization of a material and the applied magnetic field.

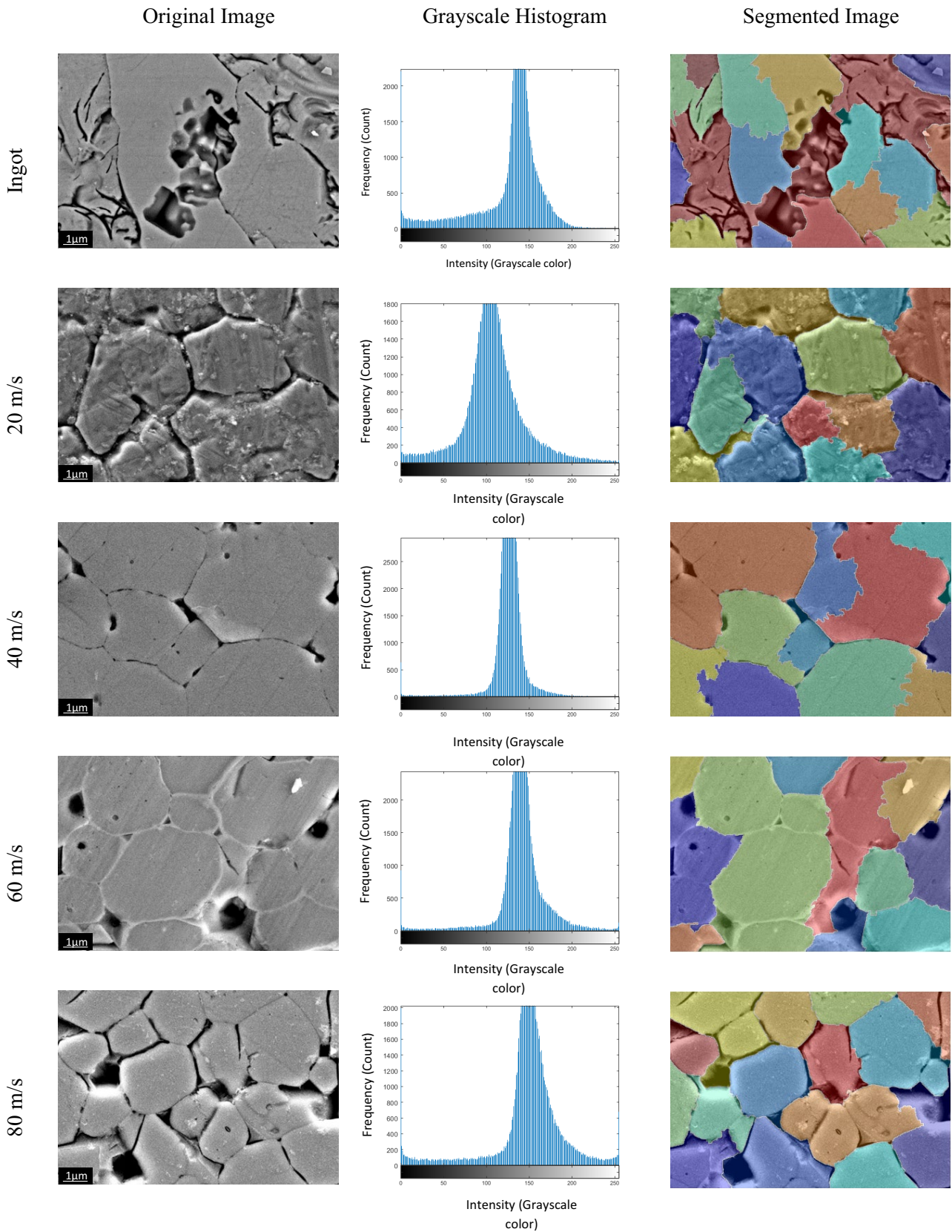


**Fig. 5** Analysis of the FE-SEM images of varying speed MS results with image histogram and image segmentation

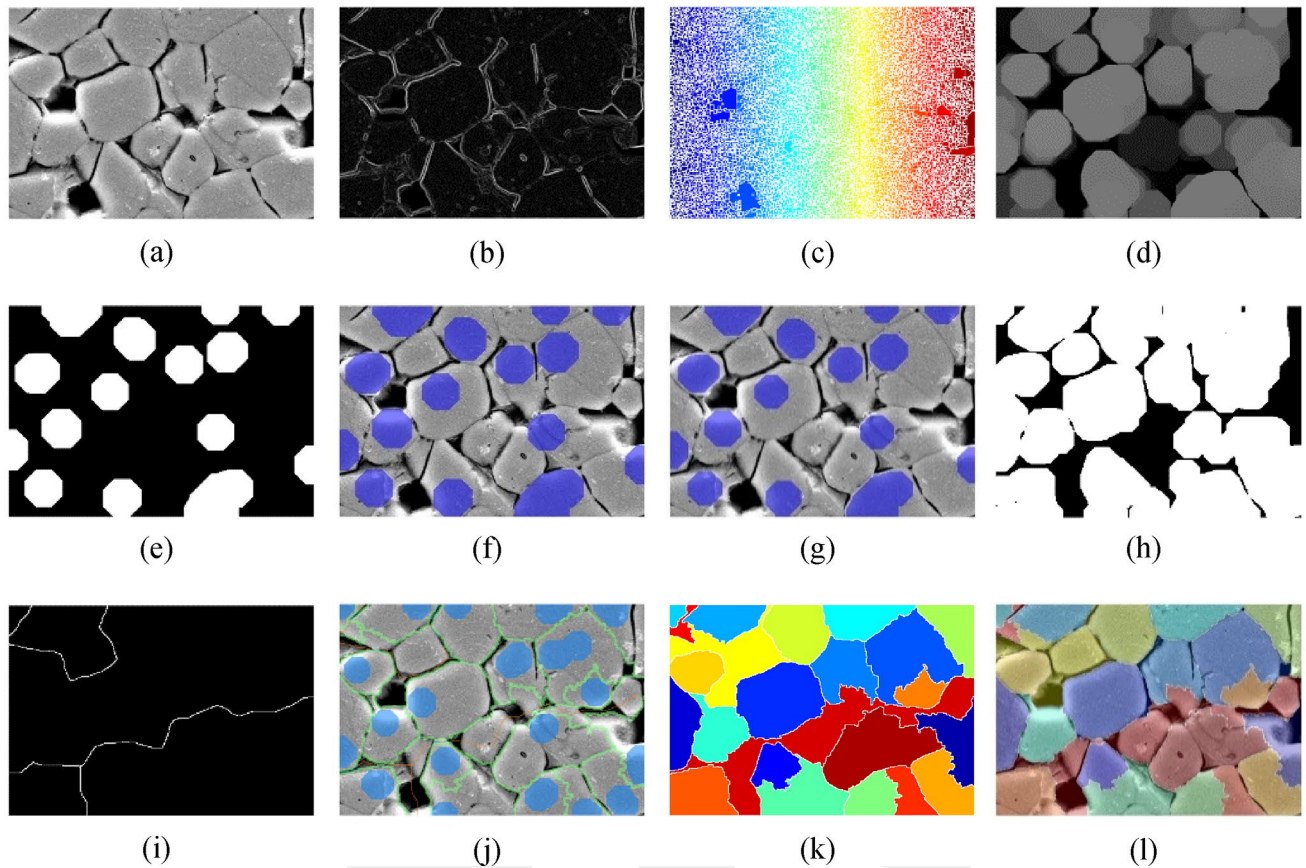


**Fig. 6** Steps of marker-controlled watershed segmentation of the 80 m/s result: **a** input image, **b** gradient magnitude, **c** initial watershed segmentation, **d** foreground object marking using morphologic opening, **e** regional maxima calculation, **f** regional

maxima on the original image, **g** modified regional maxima, **h** background extraction using binarization, **i** watershed ridge lines, **j** markers and object boundaries, **k** colored watershed labels, and **l** colored labels on the original image

The magnetization of the material increases as the applied magnetic field is increased.

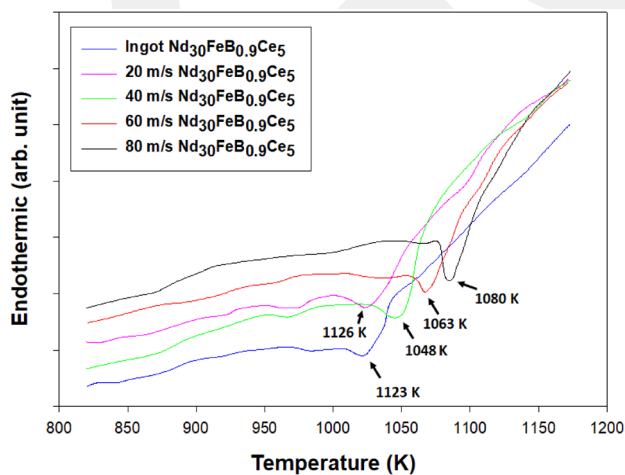


**Fig. 7** DTA melting peaks of  $\text{Nd}_{30}\text{Fe}_{65}\text{B}_{0.9}\text{Ce}_5$  alloys produced in ingot and different disc speeds

VSM analyses have been carried out to determine the magnetic properties of the  $\text{Nd}_{30}\text{Fe}_{65}\text{B}_{0.9}\text{Ce}_5$  alloys produced at different ingot and solidification rates.

The shape of the magnetic hysteresis curve provides important information about the properties of the material. In general, materials with high coercivity have steep hysteresis loops, while materials with low coercivity have flat loops. According to the hysteresis loop in Fig. 8, the sample with a disc speed of 80 m/s exhibits a better hysteresis loop than the ingot and the alloy samples at 20, 40, and 60 m/s and all samples are ferromagnetic. As the solidification rate increases, the loop area increases. The homogenization of the alloy structure and the decrease in grain size with increasing solidification rate lead to an increase in regular magnetism.

Demagnetization is the process by which the magnetization is reduced. This process can be achieved by reducing or completely eliminating the magnetic

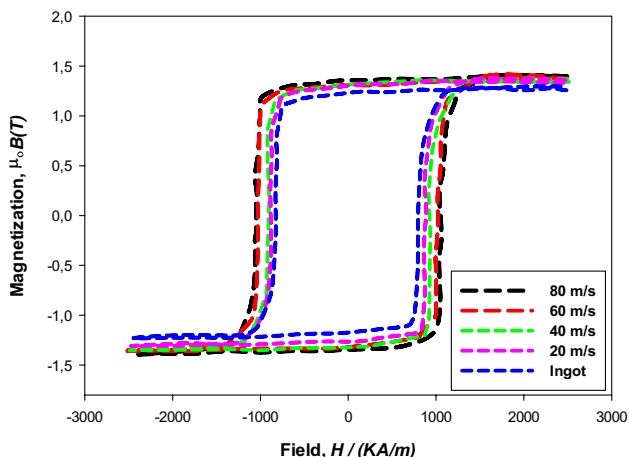


**Fig. 8** Hysteresis curves of  $\text{Nd}_{30}\text{Fe}_{65}\text{B}_{0.9}\text{Ce}_5$  alloys ingot and produced at 20,40,60, and 80 m/s disc speed

field of an object. Demagnetization is often necessary for measuring the magnetic properties of a substance or eliminating the effects of a magnetic field. Demagnetization is usually performed by applying an electromagnetic field, and the power and duration of this field can vary depending on the degree of demagnetization.

From the demagnetization curve in Fig. 9, the coercivity values of the ingot and MS samples at 20, 40, 60, and 80 are measured to be 810, 871, 932, 1011, and 1091 kA/m, respectively.

According to an ingot alloy, the coercivity value of a sample produced at a solidification rate of 80 m/s increases by approximately 34%, indicating that the

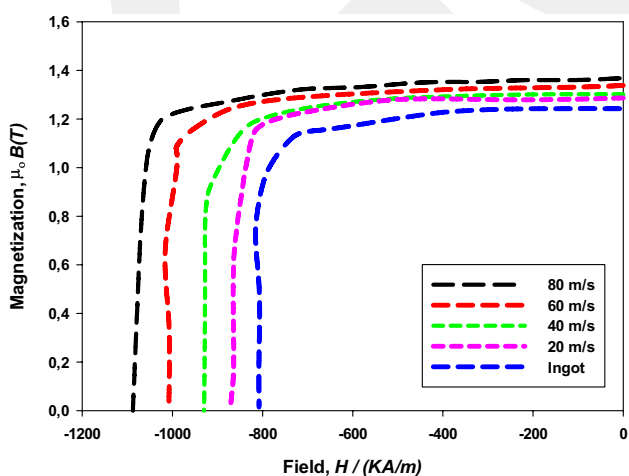


**Fig. 9** Demagnetization curve of  $\text{Nd}_{30}\text{Fe}_{65}\text{B}_{0.9}\text{Ce}_5$  alloys ingot and produced at 20, 40, 60, and 80 m/s disc speed

sample produced at a solidification rate of 80 m/s has better magnetic properties. The reason why RS alloys exhibit better magnetic properties may be due to the increase in homogeneity in the structure as well as the decrease in grain size as the solidification rate increases. Table 2 tabulates the data obtained from experimental results.

### 3.5 Mechanical properties

The microhardness results of RS ribbons are dependent on surface quality and can give very accurate results if the surface is polished using proper metallographic processes. Vickers microhardness measurements are used to determine the properties of the RS ribbons and ingot alloy in this study.

The Vickers hardness value ( $H_V$ ) is measured using an applied load of 0.098N for both the ingot and the RS specimens. The standard Vickers formula was used to calculate the values. In this test, a diamond pyramid-shaped indenter was pressed onto the surface of the material to be measured.

$H_V$  is calculated using the following formula, which incorporates the average diagonal length ( $d$ ), the indentation force ( $P$ ), and the 1.8544 geometric factor:

$$Hv = 1.8544 \times P/d^2$$

In this formula, P is the indentation force (typically chosen as 0.098 N) and d is the average diagonal length. The Vickers hardness value is used to measure the indenter resistance of the material.

The Vickers microhardness values of RS and traditional ingot alloys are presented in Table 3; it shows that the microhardness of RS strips is approximately 32% higher on average compared to the original ingot alloy. The hardness value for the  $\text{Nd}_{16}\text{Fe}_{78}\text{B}_6$  alloy is 620 Hv [31] and for the alloy sintered at 850 °C using the spark plasma sintering (SPS) method, the hardness value is 707.6 Hv [32]. In another study, the Vickers

**Table 2** Demagnetization values of ingot and alloys produced at disc speeds

Samples	$J_r$ ( $B_r$ ) (T)	$H_c$ (A/m)
Ingot	1.25	– 810
Alloy produced at 20 m/s	1.29	– 871
Alloy produced at 40 m/s	1.30	– 932
Alloy produced at 60 m/s	1.34	– 1011
Alloy produced at 80 m/s	1.37	– 1091

**Table 3** Microhardness values of ingot and alloys produced at disc speeds

Samples	Microhardness ( $H_V$ )
Ingot	$540 \pm 2.27$
Alloy produced at 20 m/s	$640 \pm 3.41$
Alloy produced at 40 m/s	$690 \pm 5.22$
Alloy produced at 60 m/s	$727 \pm 4.85$
Alloy produced at 80 m/s	$803 \pm 7.62$

hardness values of NdFeB and NdFeB + Ag magnets were measured to be 587 and 580 Hv, respectively [33].

As also mentioned in the FE-SEM analysis, compared to the grain size of the ingot alloy, the grain size of the RS strips is much smaller. Therefore, this high hardness can be attributed to the reduction in grain size and homogenization [34, 35]. Changes in the microstructure also lead to significant changes in hardness. The solidification rate and changes in the microstructure significantly increase the bending strength of the magnets.

## 4 Conclusion

This study examines the effects of rapid solidification on the structural, thermal, mechanical, and magnetic properties of  $Nd_{30}Fe_{65}B_{0.9}Ce_5$  alloys. The morphology of these alloys is greatly affected by the disc speed of the rapid solidification process as evidenced by the morphological investigation. Comparing the alloys made by ingot casting, those made at low disc speeds exhibit a more pronounced tetragonal phase structure, while those made at high disc speeds display a smaller, more homogeneous tetragonal structure. The experimental results are supported by the image histogram and segmentation analysis. The XRD analysis indicates that the XRD peak plane belongs to  $Nd_2Fe_{14}B$ , the primary phase of  $Nd_{30}Fe_{65}B_{0.9}Ce_5$  magnets. Various disc speeds cause differences in peak intensities and widths. The DTA study shows that  $Nd_{30}Fe_{65}B_{0.9}Ce_5$  samples only exhibit one endothermic melting curve which is part of the tetragonal  $Nd_2Fe_{14}B$  phase and observed between 1123 and 1180 K. According to the hysteresis curve, the sample with the best magnetic characteristics in the alloys generated at solidification rates of 20, 40, 60, and 80 is found to be the sample produced at 80 m/s. As the disc speed increases, the hysteresis conversion area also increases, and the smaller alloy structure provides

an increase in magnetism. On average, the RS samples have approximately 32% higher microhardness values compared to the original ingot alloy.

## Acknowledgements

This study has partly financed by Kayseri University Research Funds, Grant No. FYL-2022-1067 and FYL-2022-1059.

## Author contributions

OA contributed toward investigation and writing-original draft; RK contributed toward methodology and writing-review & editing; AD contributed toward writing-review & editing and resources; HC contributed toward conceptualization and methodology; and EK contributed toward resources, investigation, project administrator, and supervision.

## Funding

Open access funding provided by the Scientific and Technological Research Council of Türkiye (TÜBİTAK). This research was partially financially supported by Kayseri University Scientific Research Projects Unit (Project BAP, FYL-2022-1059).

## Data availability

The data that support the findings of this study are available from the corresponding author, upon reasonable request.

## Declarations

**Conflict of interest** The authors affirm that they have no known financial or personal conflict that would have appeared to impact the research presented in this study.

**Open Access** This article is licensed under a Creative Commons Attribution 4.0 International License, which permits use, sharing, adaptation, distribution and reproduction in any medium or format, as long

as you give appropriate credit to the original author(s) and the source, provide a link to the Creative Commons licence, and indicate if changes were made. The images or other third party material in this article are included in the article's Creative Commons licence, unless indicated otherwise in a credit line to the material. If material is not included in the article's Creative Commons licence and your intended use is not permitted by statutory regulation or exceeds the permitted use, you will need to obtain permission directly from the copyright holder. To view a copy of this licence, visit <http://creativecommons.org/licenses/by/4.0/>.

## References

1. Y. Luo, Development of NdFeB Magnet Industry in New Century. *J. Iron. Steel Res. Int.* **13**, 1–11 (2006)
2. R.H.J. Fastenau, E.J. Loenen, Applications of rare earth permanent magnets. *J. Magn. Magn. Mater.* **157**(158), 1–6 (1996)
3. K.H. Muller, G. Krabbes, J. Fink, S. Grub, A. Kirchner, G. Fuchs, L. Schultz, New Permanent Magnets. *J. Magn. Magn. Mater.* **226–230**, 1370–1376 (2001)
4. E. Burzo, M.M. Codescu, W. Kappel, E. Helerea, Magnetic materials for technical applications. *J. Optoelectron. Adv. Mater.* **11**, 229–237 (2009)
5. T. Akiya, J. Liu, H. Sepeheri-Amin, T. Ohkubo, K. Hioki, A. Hattori, K. Hono, High-coercivity hot-deformed Nd–Fe–B permanent magnets processed by Nd–Cu eutectic diffusion under expansion constraint. *Scripta Mater.* **81**(2014), 48–51 (2014)
6. W. Fan, J. Zhang, X. Liao, J. He, K. Xu, B. Zhou, H. Yu, J. Wei, Z. Liu, Preparation of hot worked dual-main phase Nd–Ce–Fe–B magnets and properties modification by grain boundary diffusion. *J. Alloy. Compd.* **922**, 166021 (2022)
7. J.F. Herbst,  $R_2Fe_{14}B$  materials: intrinsic properties and technological aspects. *Rev. Mod. Phys.* **63**, 819–898 (1991)
8. E. Niu, Z. Chen, G. Chen, Y. Zhao, J. Zhang, X. Rao, B. Hu, Z. Wang, Achievement of high coercivity in sintered R–Fe–B magnets based on misch-metal by dual alloy method. *J. Appl. Phys.* **115**, 113912 (2014)
9. L. Zhao, C. Li, Z. Hao, X. Liu, X. Liao, J. Zhang, K. Su, L. Li, H. Yu, J. Greneche, J. Jin, Z. Liu, Influences of element segregation on the magnetic properties in nanocrystalline Nd–Ce–Fe–B alloys. *Mater. Char.* **148**, 208–213 (2019)
10. Y.J. Zhang, T.Y. Ma, J.Y. Jin, J.T. Li, C. Wu, B.G. Shen, M. Yan, Effects of REFe<sub>2</sub> on microstructure and magnetic properties of Nd–Ce–Fe–B sintered magnets. *Acta Mater.* **128**, 22–30 (2017)
11. J.Y. Jin, Y.J. Zhang, G.H. Bai, Z.Y. Qian, C. Wu, T.Y. Ma, B.G. Shen, M. Yan, Manipulating Ce valence in  $RE_2Fe_{14}B$  tetragonal compounds by La–Ce Co-doping: resultant crystallographic and magnetic anomaly. *Sci. Rep.* **6**, 30194 (2016)
12. Z. Jia, M. Kou, S. Cao, X. Yang, G. Ding, S. Guo, X. Fan, B. Zheng, R. Chen, A. Yan, Effect of Nd–Co on microstructure and magnetic properties of Nd–Ce–Y–Fe–B sintered magnets. *Results in Physics* **40**, 105829 (2022)
13. M. Tokunaga, N. Meguro, M. Endoh, S. Tanigawa, H. Harada, Some heat treatment experiments for Nd–Fe–B alloys. *IEEE Trans. Magn.* **21**, 1964–1966 (1985)
14. H.A. Davies, Z.W. Liu, The influence of processing, composition and temperature on the magnetic characteristics of nanophase RE–Fe–B alloys. *J. Iron. Steel Res. Int.* **294**, 213–225 (2005)
15. Y. Putilov, A. Lukin, M. Morozova, Y. Shestak, Effect of thermal treatment on formation of high magnetic parameters of sintered magnets Nd–Fe–B. *J. Iron. Steel Res. Int.* **13**, 348–352 (2006)
16. A.A. Lukin, Influence of heat treatment parameters on properties of NdRFeMCoB sintered magnets. *J. Iron. Steel Res. Int.* **13**, 331–336 (2006)
17. L. Zhao, J. He, W. Li, X. Liu, J. Zhang, L. Wen, X. Zhang, Understanding the role of element grain boundary diffusion mechanism in Nd–Fe–B magnets. *Adv. Func. Mater.* **32**(8), 2109529 (2022)
18. X. Wang, M. Zhu, F. Xia, M. Zhang, F. Liu, Y. Guo, W. Li, Effects of grain boundary ternary alloy doping on corrosion resistance of (Ce, Pr, Nd)–Fe–B permanent magnets. *J. Rare Earth.* **39**(8), 979–985 (2021)
19. Z. Li, W. Liu, S. Zha, Y. Li, Y. Wang, D. Zhang, X. Huang, Effects of CE substitution on the microstructures and intrinsic magnetic properties of Nd–Fe–B alloy. *J. Magn. Magn. Mater.* **393**, 551–554 (2015)
20. C.J. Yan, S. Guo, R.J. Chen, D. Lee, A.R. Yan, Effect of Ce on the magnetic properties and microstructure of sintered Didymium–Fe–B magnets. *IEEE Trans. Magn.* **50**, 1–5 (2014)
21. T. Saito, Electrical resistivity and magnetic properties of Nd–Fe–B alloys produced by melt-spinning technique. *J. Alloy. Compd.* **505**, 23–28 (2010)
22. F. Chen, H. Han, T. Zhang, S. Liu, Y. Zhao, X. Wang, D. Wang, W. Zhao, Investigation of the magnetic properties, microstructure and corrosion resistance of sintered Nd–Ce–Fe–B magnets with different Ce contents. *J. Magn. Magn. Mater.* **557**, 169477 (2022)

23. S. Hirose, Y. Matsuura, H. Yamamoto, S. Fujimura, M. Sagawa, H. Yamauchi, Magnetization and magnetic anisotropy of  $R_2Fe_{14}B$  measured on single crystals. *J. Appl. Phys.* **59**, 873–879 (1986)
24. Mathworks, Histogram of image data - MATLAB imhist. Retrieved Feb 12, 2023, from <https://www.mathworks.com/help/images/ref/imhist.html>.
25. R. Kurban, A. Durmus, E. Karakose, A comparison of novel metaheuristic algorithms on color aerial image multilevel thresholding. *Eng. Appl. Artif. Intell.* **105**, 104410 (2021)
26. Mathworks, Marker-Controlled Watershed Segmentation. Retrieved Feb 12, 2023, from <https://www.mathworks.com/help/images/marker-controlled-watershed-segmentation.html>.
27. H. Zhang, Z. Tang, Y. Xie, X. Gao, Q. Chen, A watershed segmentation algorithm based on an optimal marker for bubble size measurement. *Measurement* **138**, 182–193 (2019)
28. S. Stopic, B. Polat, H. Chung, E. Emil-Kaya, S. Smiljanić, S. Gürmen, B. Friedrich, Recovery of rare earth elements through spent NdFeB magnet oxidation (first part). *Metals* **12**(9), 1464 (2022)
29. A.Z. Liu, I.Z. Rahman, M.A. Rahman, E.R. Petty, Fabrication and measurements on polymer bonded NdFeB magnets. *J. Mater. Process. Technol.* **56**(1–4), 571–580 (1996)
30. A. Lixandru, I. Poenaru, K. Güth, R. Gauß, O. Gutfleisch, A systematic study of HDDR processing conditions for the recycling of end-of-life Nd–Fe–B magnets. *J. Alloy. Compd.* **724**, 51–61 (2017)
31. M. Morishita, T. Abe, A. Nozaki, Calorimetric study of  $Nd_2Fe_{14}B$ : Heat capacity, standard Gibbs energy of formation and magnetic entropy. *Thermochim. Acta* **690**, 178672 (2020)
32. H.J. Wang, A.H. Li, M.G. Zhu, W. Li, Effect of Rare Earth Substitution on Machinability of R-Fe-B Sintered Magnets. *J. Iron. Steel Res. Int.* **13**, 367–371 (2006)
33. G.P. Wang, W.Q. Liu, Y.L. Huang, S.C. Ma, Z.C. Zhong, Effects of sintering temperature on the mechanical properties of sintered NdFeB permanent magnets prepared by spark plasma sintering. *J. Magn. Magn. Mater.* **349**, 1–4 (2014)
34. H. Chen, X. Yang, L. Sun, P. Yu, X. Zhang, L. Luo, Effects of Ag on the magnetic and mechanical properties of sintered NdFeB permanent magnets. *J. Magn. Magn. Mater.* **485**, 49–53 (2019)
35. Y. Lin, B. Wu, S. Li, S. Mao, X. Liu, Y. Zhang, L. Wang, The quantitative relationship between microstructure and mechanical property of a melt spun Al–Mg alloy. *Mater. Sci. Eng. A* **621**, 212–217 (2015)
36. G.A. Lara-Rodriguez, G. Gonzalez, H. Flores-Zúñiga, J. Cortés-Pérez, The effect of rapid solidification and grain size on the transformation temperatures of Cu–Al–Be melt spun alloys. *Mater Charact* **57**(3), 154–159 (2006)

**Publisher's Note** Springer Nature remains neutral with regard to jurisdictional claims in published maps and institutional affiliations.